Enhanced SIMO Radar System Based on Time-Frequency Correlation for Target Localization Applications

Le ZOU, Xuetian WANG, Lihua ZHANG, Hongmin GAO

Dept. of School of Integrated Circuits and Electronics, Beijing Institute of Technology, 100081, Beijing, China

zoule900818@163.com, wangxuetian@bit.edu.cn, zhanglihua2019@163.com, taoloveit@163.com

Submitted April 27, 2022 / Accepted August 22, 2022 / Online first October 7, 2022

Abstract. *This study developed a novel S-band radar system for planar location applications. High-resolution range imaging and target angle estimation were achieved by using a stepped frequency continuous wave (SFCW) signal and single input multiple output (SIMO) architecture with a linear sparse array layout, respectively. An improved time-frequency method was utilized to link the independent range profile and angle spectrum results to obtain the plane positions of the targets. The radar hardware was composed of the antenna array with one transmit element and five receive elements, an RF transceiver, and a signal processing component. Under the proposed waveform parameters and signal processing scheme, a 16-ms process cycle, 0.3-m ranging error, and 0.4° angle estimation error for target positioning were achieved in field tests. These results demonstrate the effectiveness and advantages of the proposed radar system.*

Keywords

Planar location radar, SIMO system, stepped frequency waveform, range-angle correspondence, moving target indicator, sparse array

1. Introduction

Moving target indication (MTI) technology has extensive applications in modern radar systems [1–4], especially compared to its classical use in detecting high-speed moving targets, as described by [5] and [6]. Emerging MTI technology aims at detecting slow motions such as those exhibited by civil unmanned aerial vehicles and human targets [7–9]. Slowly moving targets can also be detected by using advanced background cancellation technology [10], [11].

However, radars using MTI technology still lack real-time, fast, and high-resolution positioning and tracking. In terms of ranging, stepped frequency (SF) radar transmits a series of step-change point frequency pulses in sequence to synthesize a broadband signal and yield an ideal range resolution [12], [13]. This SF waveform has garnered considerable interest due to its wide variety of applications [14–16]. In addition, the estimation of the direction of arrival (DOA) based on single input multiple output (SIMO) or multiple input multiple output (MIMO) architecture can achieve very high angular resolution beyond the beam width generated by the array aperture [17–19].

An ultra-wideband (UWB) through-wall radar using an SF signal and a SIMO layout was proposed in [20]. This system was composed of two master/slave radars with eight switchable antenna channels. However, its target positioning was calculated by combining different range profiles of each transmit-receive pair, which required large bandwidths and only two groups of transmit-receive signals could be formed in one measurement. [21] proposed a SIMO radar system for human respiratory detection. This system combined the modified Capon algorithm with adaptive digital beam forming (ADBF) to achieve high-precision azimuth measurements in indoor settings. However, it only worked in point frequency mode and had no ranging capability. A harmonic radar proposed in [22] adopted both SF and SIMO schemes, which enabled it to achieve high resolution in range and angle dimensions simultaneously, but its receiving array was composed of several passive tags as transponders, which restricted its applications.

This study proposes an S-band target positioning radar based on time-frequency correlation processing with a stepped frequency continuous wave (SFCW) signal and SIMO architecture. The hardware composition includes an antenna array with one transmit and five receive elements, an RF transceiver module, and a signal processor controlled by an upper computer.

In view of the recently published state-of-the-art (SoA) works mentioned above, the two primary novelties and motivations of the proposed system are briefly described as follows. First, a miniaturized radar system with simplified hardware construction is proposed. Compared to the antenna switching scheme used in [20], all transmit and receive RF channels are integrated into a small metallic casing. Because all channels receive simultaneously, five groups of

DOI: 10.13164/re.2022.0468

echoes can be sampled in one measurement. Through this composite scheme, high-resolution angle measurement (such as that described in [21]) and range imaging can be accomplished simultaneously. Second, a novel time-frequency correlation signal processing method is introduced into the system. Under this combination of independently obtained range and angle results, each target's position can be determined efficiently in each stepped frequency sweep period. The results obtained in field tests demonstrate superior positioning performance and prove the effectiveness of the proposed radar scheme.

The remainder of this paper is organized as follows. First, the working mechanism and overall system architecture of the proposed radar system are introduced in Sec. 2. Then the RF transceiver and baseband signal processor (the key components) are detailed in Sec. 3 and 4, respectively. Next, Section 5 presents the human target detection experiment and signal processing results. Finally, the conclusions of this work are explained in Sec. 6.

2. Radar Mechanism and Architecture

2.1 Summary of Mechanism

The planar radar detection coordinate system is shown in Fig. 1(a). The SIMO antenna array was comprised of one transmitting and N receiving elements arranged on the x-axis. Under co-located and far field approximations, each antenna shared the same field angle. P targets in the x-y plane could be treated as several moving points, the positions of which are described in polar coordinates (r_{p}, θ_{p}), where θ_{p} denotes the azimuth (i.e., the angle between the target's position vector and the y-axis).

Under the SFCW waveform with one sweep period, which is shown in Fig. 1(b), the radar sequentially transmitted a series of point frequency pulses with frequency stepped increases from f_{L} to f_{H}. Echoes received by each channel were formed via the transmit signals experiencing a corresponding delay in the free space transmission link. Then each received echo was mixed with the transmitted signal and simultaneously sampled. For each transmitted pulse, its trailing edge time was taken as the first sampling time, and then it was moved to the left with sampling period T_{s} to obtain its In-phase/Quadrature (I/Q) sequence and incorporated baseband complex sequence according to

$$z_n(t_{j\cdot n_s}) = I_n(t_{j\cdot n_s}) + \mathrm{j}\cdot Q_n(t_{j\cdot n_s}) = \sum_{p=1}^{P} A_{p\cdot j}\cdot \mathrm{e}^{\mathrm{j}\cdot\varphi_{n\cdot p\cdot j}}, \quad (1)$$

$$A_{p\cdot j} = \frac{\sqrt{\sigma_p}\cdot G(\theta_p)\cdot c}{(4\pi)^{1.5}\cdot {r_p}^2\cdot f_j}, \quad (2)$$

$$\varphi_{n\cdot p\cdot j} = -\frac{2\pi\cdot f_j}{c}\cdot[2\cdot r_p - (x_{\mathrm{t}} + x_{\mathrm{r}n})\cdot\sin\theta_p], \quad (3)$$

$$t_{j\cdot n_s} = j\cdot\tau - (n_{\mathrm{s}} - 1)\cdot T_{\mathrm{s}}, \quad (4)$$

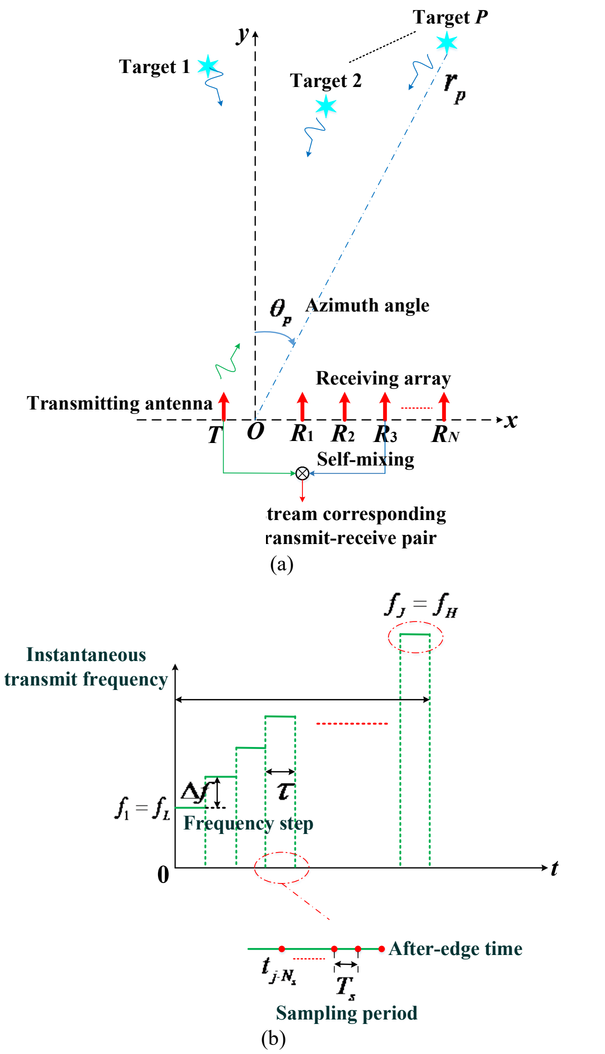

Fig. 1. (a) Radar plane detection coordinate system. (b) Diagram of the time-frequency map of the transmit waveform and sample points.

$$f_j = f_{\mathrm{L}} + (j-1)\cdot\Delta f \quad (5)$$

where c denotes the wave velocity in free space and σ_p denotes the radar cross section (RCS) of the point target p. All elements share the same gain pattern $G(\theta)$. Equation (1) indicates that the output baseband signal z_n of each receiving channel R_n was the superposition of all the signals generated by each individual target. Taking the starting time of one sweep period shown in Fig. 1(b) as $t = 0$, the sampling time corresponding to each frequency could be obtained via (4), where the after-edge time was set as the first sampling instant in each subpulse's dwell time with an order number of $n_{\mathrm{s}} = 1$. Under the SFCW waveform, the amplitude and phase of z_n (shown in (2) and (3), respectively) changed with the working frequency, which is consistent with the arithmetic sequence formula in (5). After the calibration process, which is described in Sec. 4.2, the differences between the amplitudes in all the receiving baseband signals were small, and the phase distribution indicated regular characteristics. In addition, the quasistatic observation of moving targets could be achieved using a reasonably short sweep period. Therefore, the velocities of the targets were not considered in (1)–(3), which resulted in the amplitude and phase described in (2) and (3), respectively, being dependent only on the frequency f_j. Within the given dwell time of the SF subpulse, the complex signal represented by (1) could be regarded as a time-invariant term.

In the signal model shown in (1)–(3), only the transmission delay experienced in free space was considered, as the additional phase shift caused by the radar antenna and target was not included. The influences of such phase information loss were analyzed through the following process. First, the RF signals at the ports of the transmitting and receiving antennas were taken as the input and output signals, respectively, and then the transceiver link was modeled as a two-port network. As the broadband SF signal contained a series of spectral components of point frequency subpulses used in the system, the accurate phase of the complex signal in (1) corresponding to different frequencies f_j could be expressed by the group delay of the network, where the constant term, linear distortion, and quadratic term distortion were considered as they are in engineering generally. Within the given bandwidth, the distortion caused by the change of carrier frequency could be suppressed through reasonable group delay filter design, such as that in [23]. On this basis, a simple correction process could be performed on the peak shift in the range profile to offset the constant group delay caused by the antenna and target. Empirically, for typical human target ranging, the absolute value of the error requiring correction is usually less than 1 m.

2.2 System Hardware Composition

The block diagram of the proposed radar system is illustrated in Fig. 2. Similar to the generally adopted architecture (such as that described in [21] and [24]), this system was composed of an antenna array, transceiver, signal processor, and upper computer. The RF front end generated a SFCW signal, which was delivered equally to the transmit channel and the local oscillators to output the mixed baseband signal corresponding to each receive channel (the corresponding theoretical formula is shown in Sec. 2.1). Then each baseband signal composed of two I/Q branches were fed into the signal processor module to complete the positioning measurement in one sweep period. To balance

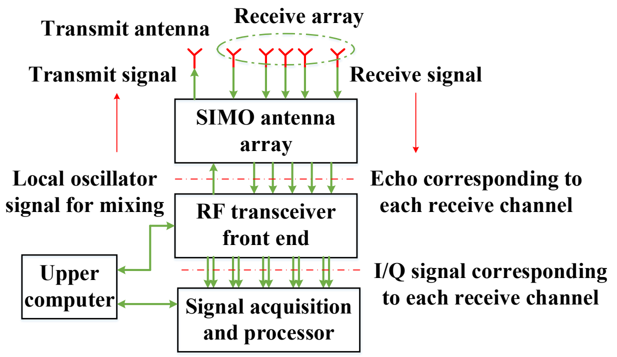

Fig. 2. Block diagram of the hardware configuration in the proposed system.

the cost and performance, the number of receiving channels N was selected to be 5. All procedures mentioned above were unified and controlled by the upper computer.

3. RF Waveform and Components

3.1 Radar Waveform Parameters

As mentioned above, this system achieved high-resolution range imaging by using an SFCW signal. The elements used to define the waveform parameters are now described. First, the radar's working band was selected to be 3.1–3.42 GHz (the S-band) with a range resolution of approximately 0.5 m; this frequency range is widely used for human target detection. Second, the detectable range of the radar system was determined by three factors: the maximum radar range $R_{\max}$ determined by the radar equation,

$$R_{\max} = \left[\frac{P_t \cdot \tau \cdot G^2 \cdot \lambda_c^2 \cdot \sigma \cdot J \cdot N_s}{(4\pi)^3 \cdot S_{i\min}} \right]^{\frac{1}{4}}, \tag{6}$$

the range bin in the inverse fast Fourier transform (IFFT), and the unambiguous range determined by the pulse width τ in

$$R_u = \min\left(\frac{c}{2 \cdot \Delta f}, \frac{c \cdot \tau}{2}\right). \tag{7}$$

Based on the detectable range and the requirement of quasistatic measurement for slow moving targets, the final set of working parameters used in this study is shown in Tab. 1.

3.2 RF Front-end Prototype

Figure 3(a) shows a schematic of the proposed transceiver and Figure 3(b) shows an image of the prototype. The RF front end consisted of three basic parts: a frequency synthesizer, transmitter, and receiver. The frequency synthesizer generated the baseband SFCW and a 3-GHz point frequency signal through the direct digital synthesizer (DDS), integration of the phase-locked loop (PLL), and voltage-controlled oscillator (VCO), respectively, which were then mixed and bandpass filtered (BPF) to generate the

Parameter	Symbol	Value and Unit
Band	$f_L - f_H$	(3.1–3.42) GHz
Frequency step	Δf	1 MHz
Frequency number	J	321
Pulse width	τ	50 µs
Antenna gain	G	10 dBi
Center wavelength	λ_c	92 mm
Receiver sensitivity	$S_{i\min}$	–90 dBm
Sampling rate	f_s	4 MHz
Sampling points in each pulse	N_s	100
Number of receiving channels	N	5

Tab. 1. Summary of radar operating parameters.

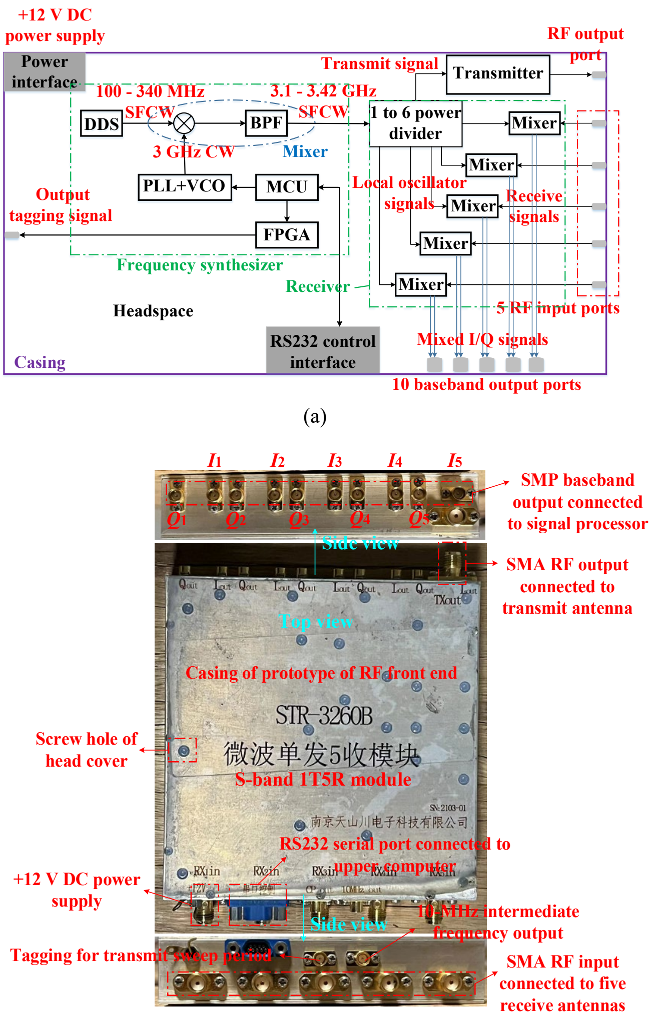

Fig. 3. (a) Schematic of the proposed transceiver and (b) image of the prototype of the proposed transceiver.

required RF SFCW signal. A microcontroller unit (MCU) connected the upper computer through an RS232 interface and also produced the tagging signal, which appeared as a high-level pulse with width τ at each frame's starting time and marked each transmit sweep cycle through the field programmable gate array (FPGA). The signal generated by the frequency synthesizer was then divided into six identical and time-synchronized signals through the power divider and sent to the transmitter and receiver. Then these resultant signals worked as the local oscillator signals in the transmitter and receiver for mixing and generating ten baseband I/Q signals.

4. Signal Processing

4.1 Overall Procedure

The processing flow performed on the I/Q signal output from the RF front end is shown in Fig. 4. Based on the transmit tagging signal and time sequence, the procedure was divided into three parts: sampling, pretreatment, and

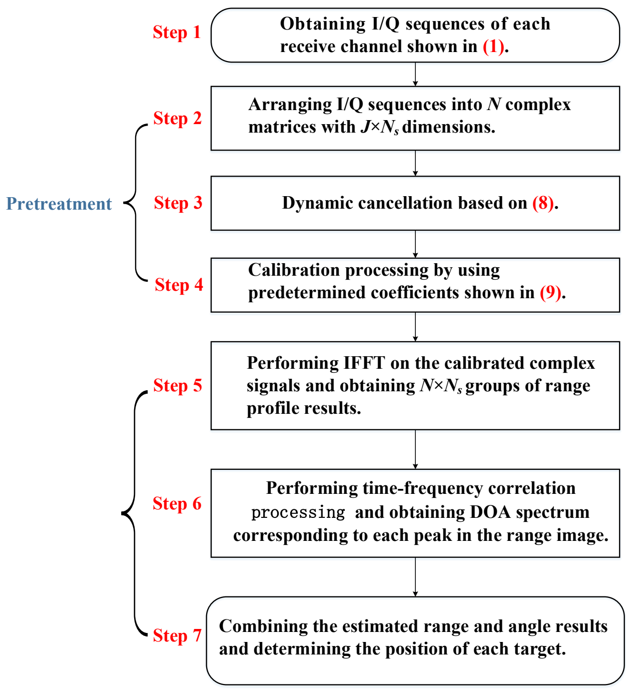

Fig. 4. Overall procedure of signal processing for the proposed radar in one transmit SFCW sweep period.

position estimation from the measured data. The data points were selected in each transmit sweep period by the tagging signal, as shown in Figs. 1(b) and (4). The pretreatment and positioning are described in Sec. 4.2 and 4.3, respectively.

4.2 MTI and Calibration Processing

Before conducting positioning measurements, it was necessary to preprocess the arranged I/Q signal matrices. First, MTI processing of dynamic cancellation was performed to extract moving targets from stationary background clutters based on their Doppler frequency differences. The cancellation method was conducted in consecutive multiple cycles and was represented in multiple frames as

$$\begin{cases} y_k = \alpha \cdot y_{k-1} + (1-\alpha) \cdot x_k, \\ z_k = x_k - y_k \end{cases} \tag{8}$$

where x_k, y_k, and z_k denote the total baseband signal, the signal generated by the background, and the signals generated by the targets, respectively, corresponding to the same receiving channel in frame k. The cancellation factor α was set to 0.8 for processing. Taking the I/Q signal sampled in a certain frame within the observation time as the initial background data, the background and target data of each subsequent frame were recursively processed via (8). The dynamic cancellation method used here was aimed at extracting the echoes of the moving targets. As the observation time increased, the number of range imaging frames with gradually highlighted range profile peaks corresponding to slowly moving targets increased, while the stationary objects were treated as clutter and filtered out.

The setup of the calibration scenario is shown in Fig. 5(a). In contrast to the point frequency CW used in [21], this calibration was conducted under synchronous transmit and local oscillator SFCW signals controlled by the upper computer. For the detection of the far-field point target shown in Fig. 1(a), the field of view (FOV) of each antenna was uniformly referenced to the target's azimuth angle. In this ideal approximation, when the target was located on the y-axis with a 0° azimuth angle, the echo received by each receiving element should have the same amplitude and phase according to (2) and (3). However, the amplitudes and phases of each output I/Q signal were unequal due to the differences in position between each receiving element. The purpose of the calibration was to obtain all receiving I/Q complex signals with an ideal uniform phase and amplitude distribution for the signals incident from 0° according to the established radar coordinate and SIMO array layout shown in Fig. 5(a).

In order to minimize the influence of interference signals, the calibration was performed in an anechoic chamber. A single input single output (SISO) radar, which had a transmitting antenna with a main lobe facing the y-axis, was used as the signal source to transmit SF signals to the calibrated SIMO radar. At the receiving end of the SIMO radar, the SF signals received by five receiving antennas were mixed with local oscillator (LO) signals and low-pass filtered to generate the corresponding I/Q signals. All unused elements were connected to coaxial attenuators and matched loads. For imitating the Doppler frequency difference caused by the target motion in the actual setting, a 20-Hz frequency difference between the transmit and LO signals corresponding to a 1-m/s radial velocity and a 3-GHz carrier frequency were set, as shown in Fig. 5(b). J FFT iterations corresponding to each stepped frequency's dwell time of N receive channels were performed on the sampled sequence. The dwell time τ of each SF subpulse was set to 100 ms to obtain an FFT spectral resolution of up to 10 Hz. The amplitude and phase of the spectrum at the Doppler frequency were denoted as $a_{n\cdot j}$ and $\varphi_{n\cdot j}$, respectively; after MTI processing, these were used to calibrate the complex signals according to

$$z_n^{'}(t_{j\cdot n_s}) = \frac{e^{-j\varphi_{n\cdot j}}}{a_{n\cdot j}} \cdot z_n(t_{j\cdot n_s}). \tag{9}$$

Taking the dwell time of the first SF subpulse in Fig. 5(b) as an example, the in-phase component sampling sequences generated by each receiving channel during this time with and without calibration are shown in Fig. 6. All the presented signals had their direct current component removed and were normalized. Before calibration, there was a certain amount of imbalance in the amplitude and phase of the output signal from each receiving channel for the incident direction of 0°. After calibration, the relationship between the amplitude and phase of the sampled signal in different channels could be approximated by

$$I_n(t_{j\cdot n_s}) = \cos\left[2\pi f_d \cdot t_{j\cdot n_s} - 2\pi(f_j + f_d)\cdot\frac{R}{c}\right] \tag{10}$$

where f_d denotes the Doppler frequency shift between the transmit and LO SF signals, t_{jn_s} is the sampling instant during each subpulse's dwell time in (1), and R denotes the distance from the transmitting antenna of the SISO radar to the coordinate origin.

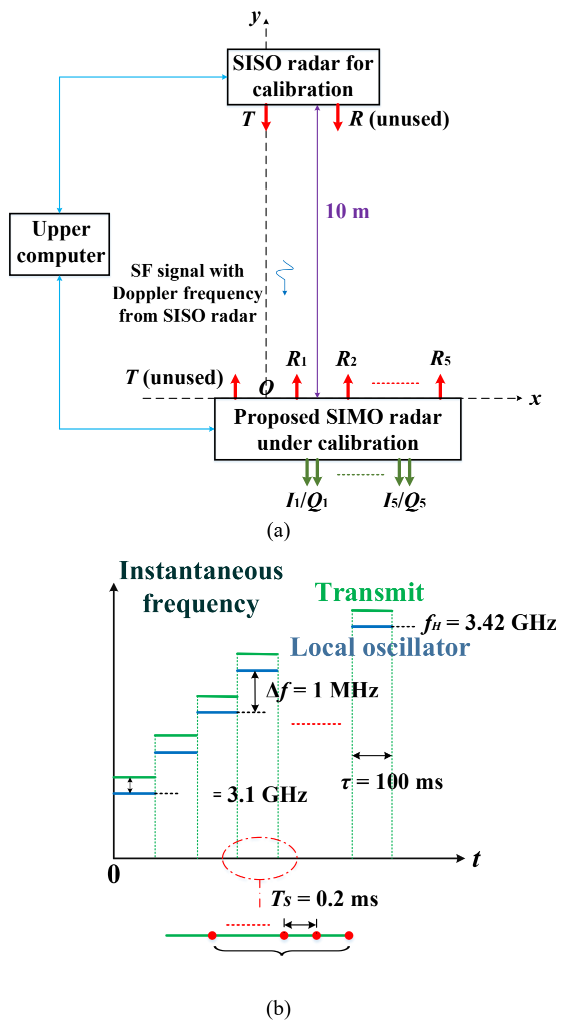

Fig. 5. Schematics of the waveform parameter setups in the calibration process. (a) Diagram and (b) SF signal at the transmit and receive ends.

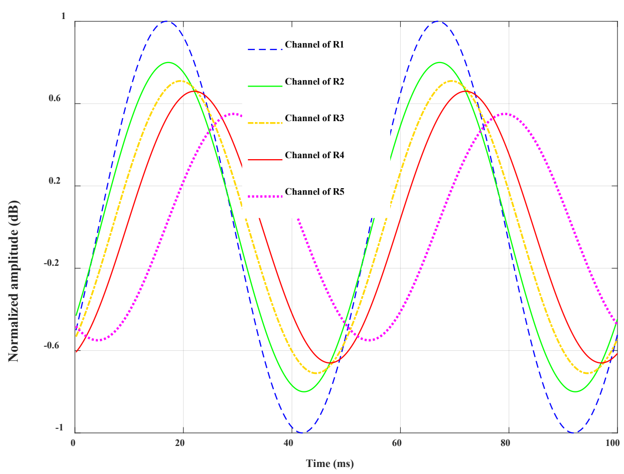

(a)

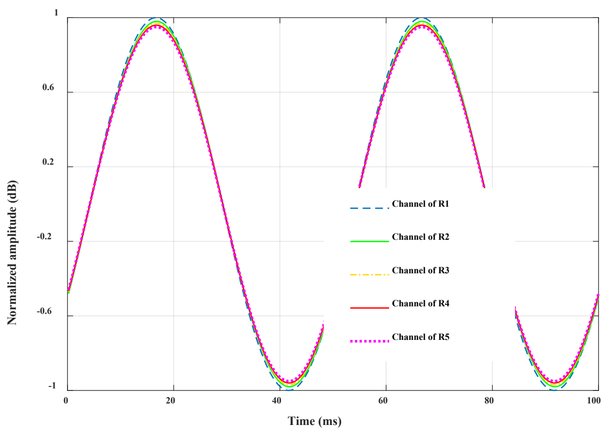

(b)

Fig. 6. Examples of waveforms in the in-phase component signal calibration. (a) Before calibration and (b) after calibration.

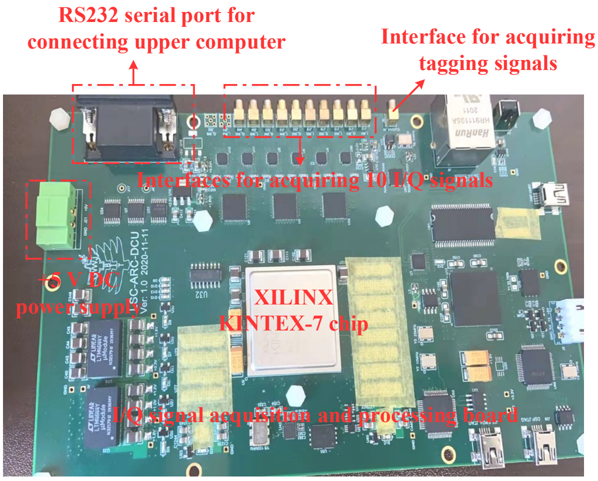

Fig. 7. Prototype of the baseband signal acquisition and processing circuit board.

4.3 Target Localization

In this scheme, the high range resolution achieved by the SFCW signal and the capability of resolving coherent sources via the modified Capon algorithm described in [21] were jointly utilized, and an improved time-frequency correlation positioning method was further developed. For the measurement in each frame, the first step was to perform IFFT on the calibrated baseband sampling sequence in each receiving channel according to (9) and obtain $N \times N_S$ groups of range profiles in the time domain, ideally with high consistency. Second, for each target peak point in the profile, windowing was conducted to filter profiles that included only one range peak, which were then transformed back into the frequency domain via FFT. At this time, the baseband sequences only included the components corresponding to a single range. Next, the modified Capon DOA algorithm was applied to the sequences of each point frequency pulse and each single range. Then the covariance matrix and angle spectrum at each frequency point were obtained according to

$$\hat{R}(f_j) = \frac{1}{N_s} \cdot \sum_{n_s=1}^{N_s} \mathbf{z}'(t_{j \cdot n_s}) \cdot \mathbf{z}'(t_{j \cdot n_s})^{\mathrm{H}} \tag{11}$$

and

$$P(\theta, f_j) = \frac{1}{\mathbf{a}^{\mathrm{H}}(\theta, f_j) \cdot \hat{R}^{-\upsilon}(f_j) \cdot \mathbf{a}(\theta, f_j)}, \tag{12}$$

respectively, where $\mathbf{z}$ denotes the column vector arranged by the complex signals of all receiving channels, $\mathbf{a}$ is a steering vector determined by the array layout, and υ is an integer that is set to 5 in actual applications. After the calculation via (12), the spectrum of each frequency point was averaged to obtain the formula estimating the final spectrum. Solving each range peak using the abovementioned time-frequency correlation method enabled the position of each target to be determined. The measurements under this scheme and the results for three human targets are discussed in Sec. 5.

4.4 Hardware Implementation

Figure 7 shows the prototype of the baseband signal acquisition and processing circuit board developed using the commercial XILINX KINTEX-7 chip and FPGA technology. In addition to the ten I/Q acquisition ports, this board also included the transmit tagging signal acquisition port and RS232 interface for control by the upper computer, which allowed the sampling rate to be adjusted and each individual port to be activated.

5. Field Test and Discussion of Results

Based on the proposed radar system with the working parameters shown in Tab. 1 and the signal processing scheme introduced in Sec. 4, the human target positioning experiment was conducted, as shown in Fig. 8(a). Under the established coordinate system, the three human targets were asked to stand at different initial positions and move in different directions with a speed of about 1 m/s. The radar executed a transmit sweep period of about 16 ms as its time handling frame. To highlight the positioning performance for moving targets, the measured results of the frames at about 1 s and 3 s were observed, as shown in Figs. 8(b) and (c). For simplicity of presentation, only the range profiles corresponding to the trailing edge of each pulse and the R_1 receiving channel are shown in Fig. 8(b). In addition, in order to improve the resolution performance of the array, a sparse layout based on the ambiguity function optimization, such as that in [25], was used in this system.

Considering the difficulties in simulating the complex clutter environment in the test, here we directly give the measured data. The ten I/Q signals were sampled by the baseband board shown in Fig. 7 and imported into the upper computer (a laptop) for processing. As shown in Fig. 8(b), the three targets could be distinguished in the range profiles of both frames. For each range peak, a rectangular window with a width identical to the range resolution was adopted to obtain each target's angle spectrum, as shown in Fig. 8(c). The latter clearly reflects the motion between the two frames.

Because average processing was used for the angular spectrum corresponding to the 321 frequency points, the fluctuations in the curves shown in Fig. 8(c) are small. In contrast, for the range profile shown in Fig. 8(b), fluctuations of approximately 10 dB appear outside the target peak because there was only one snapshot included in each pulse. Linking the six range peaks and six angle peaks in the two images enabled the positioning results of these two frames to be obtained. An interval scale of 0.1° was used for the angle axis of the DOA spectrum. Based on the normalized curves shown in Figs. 8(b) and (c), peak searches with –5 dB and –3 dB thresholds were performed to estimate each target's range and azimuth angle, respectively. A comparison between the presupposed accurate results and the estimated results obtained from the range profiles and angle spectra is summarized in Tab. 2. As can be derived from the table, the maximum error occurred in the range and angle estimation in two observed frames at about 0.3 m and 0.4°, respectively, which resulted in a relative ranging error of less than 2%.

Furthermore, a comparison between other similar works is summarized in Tab. 3. From the perspective of applications, the proposed system is different from other radars listed in Tab. 3 in terms of the design and performance because it is a positioning radar used to detect slow-moving targets such as human beings. Because the ranging resolution of SF radar is proportional to the signal bandwidth, a high ranging resolution can be achieved by developing millimeter wave and terahertz radar, such as those described in [15] and [24]. Compared to the large bandwidth characteristics presented in [15] and [24], the proposed radar works in the microwave S-band with a bandwidth of only 320 MHz, which qualifies its range resolution as acceptable for practical applications. Second, compared to the 2-D FFT imaging used in the UWB through-wall radar proposed in [20], this system adopted an efficient time-frequency correlation positioning method, which significantly simplified the signal processing complexity and increased the resolution in the longitudinal and cross-range directions of the radar coordinate system. Third, in contrast to the method of adopting long observation times to obtain high Doppler frequency resolution, such as was

	Frame at 1 s		Frame at 3 s	
	Presupposed position	Estimated position	Presupposed position	Estimated position
Target 1	15.21 m, –9.5°	15.4 m, –9.7°	15.66 m, –16.7°	15.81 m, –17.1°
Target 2	14 m, 0°	13.77 m, 0°	12 m, 0°	11.7 m, 0.1°
Target 3	16.07 m, 5.35°	16.35 m, 5.4°	18.06 m, 4.8°	18.31 m, 4.7°

Tab. 2. Summary of presupposed and estimated target positions.

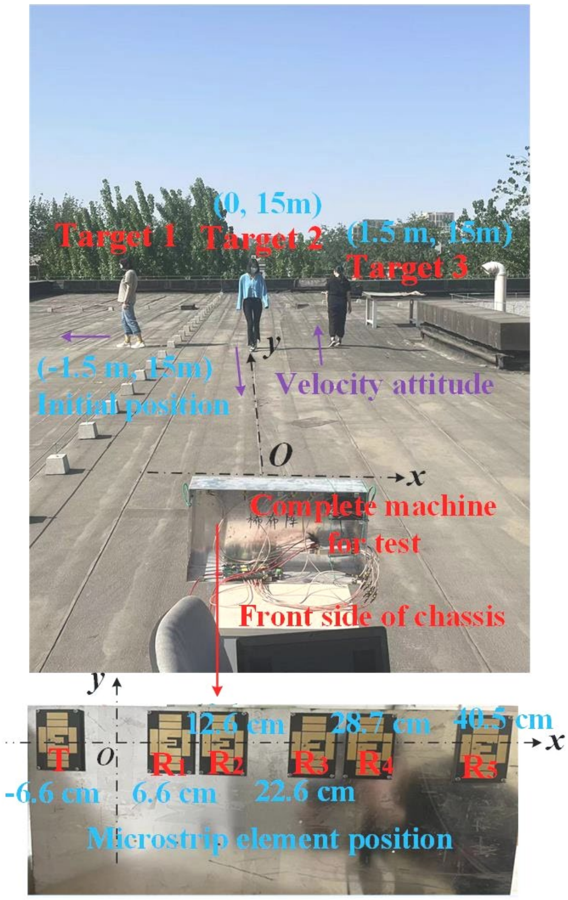

(a)

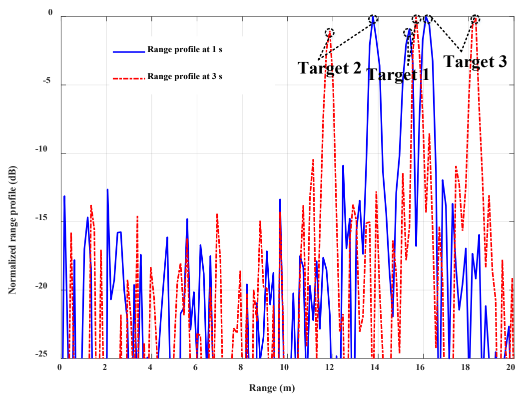

(b)

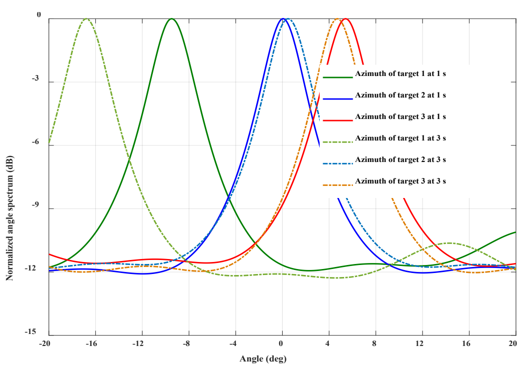

(c)

Fig. 8. (a) Image of field test. (b) Range profiles from field test data. (c) Angle spectra from field test data.

Ref.	Working band	Waveform	Measurement	Array structure	Resolution	Measurement error	Frame length
[15]	29.7–32.88 GHz	SFCW	Range imaging	SISO	0.05 m in ranging	0.0051 m in ranging	Not given
[16]	8.5–9.5 GHz	SFCW	2-D FFT for range-Doppler mapping	SISO	0.15 m in ranging, 0.2 Hz in Doppler frequency	≤ 0.1 m in ranging, ≤ 0.1 Hz in Doppler frequency	10.1 s
[20]	1–4 GHz	SFCW	2-D FFT imaging	SIMO	0.05 m in ranging, 0.63 m in cross ranging	0.1 m in ranging, 0.5 m in cross ranging	Not given
[21]	5.8 GHz	CW	DOA + ADBF and FFT for Doppler mapping	SIMO	15° in DOA, better than 0.4 Hz in Doppler frequency	6° in DOA, ≤ 0.05 Hz in Doppler frequency	≥ 2.5 s
[24]	121–127 GHz	FMCW + CW	Ranging by combined frequency and phase evaluation	SISO	0.05 m in ranging	60 μm in ranging	15.93 ms
[26]	2.4 GHz	CW	2-D DBF and FFT for Doppler mapping	MIMO	17° in DBF, better than 0.15 Hz in Doppler frequency	1.5° in DBF, 0.02 Hz in Doppler frequency	≥ 6.67 s
This work	3.1–3.42 GHz	SFCW	Range imaging and time-frequency correlation DOA	SIMO	0.47 m in ranging, 4.7° in DOA	0.3 m in ranging, 0.4° in DOA	16 ms

Tab. 3. Comparison with other radar systems.

done in [16], [21], and [26], the main task of this system was to detect slow-moving targets rather than perform Doppler frequency measurements. Hence, a compromise between minimizing the frame length for fast positioning and tracking and maximizing the radar range described in (6) and (7) was considered in the design. Under this improved time-frequency correlation scheme, the proposed system could achieve fast and highly accurate positioning with a limited bandwidth and a low hardware cost.

6. Conclusion

This paper presented an S-band planar positioning radar system that used an SFCW signal and SIMO architecture. The hardware structure was simplified into a sparse antenna array, RF front end, and signal processing module. A time-frequency correlation method based on joint IFFT range imaging and the modified Capon algorithm was adopted in the signal processing module. By windowing each target peak in multiple groups of range profiles and returning to the frequency domain for the DOA algorithm, the angle corresponding to each target range could be found one by one. The processing step used the frequency sweep cycle as the basic time step and resulted in a positioning time of about 16 ms. Superior positioning performance with a ranging error of about 0.3 m and an angle estimation error of 0.4° were achieved in a field test. These results confirmed the effectiveness of the proposed radar system and its excellent prospects in applications requiring fast locating and tracking.

References

[1] MA, Y. G., HONG, H., ZHU, X. H. Multiple moving-target indication for urban sensing using change detection-based compressive sensing. *IEEE Geoscience and Remote Sensing Letters*, 2021, vol. 18, no. 3, p. 416–420. DOI: 10.1109/LGRS.2020.2977168

[2] CEBA, F., MAKHOUL, E., BROQUETAS, A., et al. Modeling fast boat motion impact on satellite SAR MTI systems. *IEEE Geoscience and Remote Sensing Letters*, 2015, vol. 12, no. 10, p. 2145–2149. DOI: 10.1109/LGRS.2015.2453018

[3] LI, J. A., ZHU, X. M., STOICA, P., et al. High resolution angle-Doppler imaging for MTI radar. *IEEE Transactions on Aerospace and Electronic Systems*, 2010, vol. 46, no. 3, p. 1544–1556. DOI: 10.1109/TAES.2010.5545209

[4] LI, K., WEN, B. Y., XU, Y. M., et al. A novel UHF radar system design for river dynamics monitoring. *IEICE Electronic Express*, 2015, vol. 12, no. 4, p. 1–8. DOI: 10.1587/elex.12.20141074

[5] LAGERKVIST, L. Design considerations for a modern naval fire control radar. In *IEEE Radar Conference*. Arlington (USA), 2010, p. 615–619. DOI: 10.1109/RADAR.2010.5494547

[6] SACHUK, I. I., ORLENKO, V. M., SHIRMAN, Y. D. UWB signals, SA perspectives in radar guidance. In *3rd International Conference on Ultrawideband and Ultrashort Impulse Signals (UWBUS)*. Sevastopol (Ukraine), 2006, p. 133–135. DOI: 10.1109/UWBUS.2006.307179

[7] GUO, J. P., CHANG, S. Q., YANG, F. W., et al. Low-slow-small target detection using stepped-frequency signals in a strong folded clutter environment. *IET Radar Sonar and Navigation*, 2021, vol. 15, no. 9, p. 1030–1044. DOI: 10.1049/rsn2.12095

[8] WANG, K., ZENG, Z. F., SUN, J. G. Through-wall detection of the moving paths and vital signs of human beings. *IEEE Geoscience and Remote Sensing Letters*, 2019, vol. 16, no. 5, p. 717–721. DOI: 10.1109/LGRS.2018.2881311

[9] CHEN, H. Y., LIU, Y. X., JIANG, W. D., et al. A new approach for synthesizing the range profile of moving targets via stepped-frequency waveforms. *IEEE Geoscience and Remote Sensing Letters*, 2006, vol. 3, no. 3, p. 406–409. DOI: 10.1109/LGRS.2006.873874

[10] XIA, Y., NING, S., SHEN, H., Moving targets detection algorithm based on background subtraction and frames subtraction. In *The 2nd International Conference on Industrial Mechatronics and Automation (ICINDMA)*. Wuhan (China), 2010, p. 122–125. DOI: 10.1109/ICINDMA.2010.5538075

[11] BAO, Y., REN, L., HE, P., et al. A novel approach for clutter cancellation in HPRF stepped-frequency radar. In *9th International Conference on Signal Processing (ICOSP)*. Beijing (China), 2008, p. 2384–2387. DOI: 10.1109/ICOSP.2008.4697629

[12] YBARRA, G., WU, S., BILBRO, G., et al. Optimal signal processing of frequency-stepped CW radar data. *IEEE Transactions on Microwave Theory and Techniques*, 1995, vol. 43, no. 1, p. 94–105. DOI: 10.1109/22.363002

[13] AUBRY, A., CAROTENUTO, V., DE MAIO, A., et al. High range resolution profile estimation via a cognitive stepped frequency technique. *IEEE Transactions on Aerospace and Electronic Systems*, 2019, vol. 55, no. 1, p. 444–458. DOI: 10.1109/TAES.2018.2880024

[14] REN, L., KONG, L., FOROUGHIAN, F., et al. Comparison study of noncontact vital signs detection using a Doppler stepped-frequency continuous-wave radar and camera-based imaging photoplethysmography. *IEEE Transactions on Microwave Theory and Techniques*, 2017, vol. 65, no. 9, p. 3519–3529. DOI: 10.1109/TMTT.2017.2658567

[15] PARK, J., NGUYEN, C. A new millimeter-wave step-frequency radar sensor for distance measurement. *IEEE Microwave and Wireless Components Letters*, 2002, vol. 12, no. 6, p. 221–222. DOI: 10.1109/LMWC.2002.1010001

[16] SU, W. C., TANG, M. C., EL ARIF, R., et al. Stepped-frequency continuous-wave radar with self-injection-locking technology for monitoring multiple human vital signs. *IEEE Transactions on Microwave Theory and Techniques*, 2019, vol. 67, no. 12, p. 5396 to 5405. DOI: 10.1109/TMTT.2019.2933199

[17] KAKOUCHE, I., ABADLIA, H., EL KORSO, M. N., et al. Joint vital signs and position estimation of multiple persons using SIMO radar. *Electronics*, 2021, vol. 10, no. 22, p. 1–15. DOI: 10.3390/electronics10222805

[18] XIONG, J. J., HONG, H., XIAO, L., et al. Chest and abdominal signals separation based on SIMO radar with difference beamforming. *IEEE Microwave and Wireless Components Letters*, 2022, vol. 32, no. 3, p. 218–221. DOI: 10.1109/LMWC.2022.3144502

[19] FRIENDLANDER, F. On the relationship between MIMO and SIMO radars. *IEEE Transactions on Signal Processing*, 2009, vol. 57, no. 1, p. 394–398. DOI: 10.1109/TSP.2008.2007106

[20] BOUTTE, D., LEE, H., RADZICKI, V., et al. A portable SIMO radar for through wall detection and imaging. In *IEEE Military Communications Conference (MILCOM)*. Tampa (USA), 2015, p. 204–209. DOI: 10.1109/MILCOM.2015.7357443

[21] XIONG, J. J., HONG, H., ZHANG, H. Q., et al. Multitarget respiration detection with adaptive digital beamforming technique based on SIMO radar. *IEEE Transactions on Microwave Theory and Techniques*, 2020, vol. 68, no. 11, p. 4814–4824. DOI: 10.1109/TMTT.2020.3020082

[22] HEUERMANN, H., HARZHEIM, T., CRONENBROECK, T. First SIMO harmonic radar based on the SFCW concept and the HR transfer function. *Remote Sensing*, 2021, vol. 13, no. 24, p. 1 to 23. DOI: 10.3390/rs13245088

[23] LAI, X. P., LAI, C. L., ZHAO, R. J. An iterative approach to near-uniform group-delay error design of FIR filters. *IEEE Signal Processing Letters*, 2011, vol. 18, no. 2, p. 107–110. DOI: 10.1109/LSP.2010.2099217

[24] PAULI, M., GOTTEL, B., SCHERR, S., et al. Miniaturized millimeter-wave radar sensor for high-accuracy applications. *IEEE Transactions on Microwave Theory and Techniques*, 2017, vol. 65, no. 5, p. 1707–1715. DOI: 10.1109/TMTT.2017.2677910

[25] VASANELLI, C., BATRA, R., DI SERIO, A., et al. Assessment of a millimeter-wave antenna system for MIMO radar applications. *IEEE Antennas and Wireless Propagation Letters*, 2017, vol. 16, p. 1261–1264. DOI: 10.1109/LAWP.2016.2631889

[26] FENG, C., JIANG, X. N., JEONG, M. G., et al. Multitarget vital signs measurement with chest motion imaging based on MIMO radar. *IEEE Transactions on Microwave Theory and Techniques*, 2021, vol. 69, no. 11, p. 4735–4747. DOI: 10.1109/TMTT.2021.3076239

About the Authors ...

Le ZOU (corresponding author) was born in Beijing, China in 1990. He received his B.Sc. from Yanshan University, Qinhuangdao, China, in 2013, and M.Sc. degrees from the Beijing University of Posts and Telecommunications, Beijing, China, in 2017. He is currently enrolled in the Ph.D. program in the School of Information and Electronics, Beijing Institute of Technology. His research interests include antenna theory and design, millimeter wave radar technology, and monopulse detection systems.

Xuetian WANG was born in Yangzhou, China. He received his Ph.D. from the Beijing Institute of Technology in 2002. He is currently a Professor in the Department of School of Integrated Circuits and Electronics, Beijing Institute of Technology, Beijing, China. His research interests include computational electromagnetics, electromagnetic compatibility measurement techniques, terahertz radar technology, and millimeter wave remote sensing and imaging technology.

Lihua ZHANG was born in Shijiazhuang, China. She received her B.Sc. from Hebei University of Technology. She is currently working toward her M.Eng. degree in Electronics and Information at the Beijing Institute of Technology. Her research interests include antenna design and radar technology.

Hongmin GAO was born in Tangshan, China. He received his Ph.D. from the Beijing Institute of Technology. He is currently an Associate Professor in the Department of School of Integrated Circuits and Electronics, Beijing Institute of Technology, Beijing, China. His research interests include radio frequency circuit design, navigation guidance and control, and electromagnetic compatibility measurement techniques.